AIAA JOURNAL
Vol. 56, No. 4, April 2018

Bi-Directional Stiffness for Airfoil Camber Morphing

Matthew DiPalma* and Farhan Gandhi†
Rensselaer Polytechnic Institute, Troy, New York 12180

DOI: 10.2514/1.J056629

This paper explores a new design for an airfoil whose chordwise bending stiffness varies with direction of applied load. By designing the region aft of the spar to be very stiff under upward load, uncommanded camber deformation under aerodynamic pressure can be minimized. At the same time, lower stiffness under reversed load reduces actuation requirement to achieve a desired downward camber deformation. Rigid cantilevers extending from the rear of the spar toward the trailing edge, and flush with the lower skin are used to realize this goal. Under upward load the rigid cantilever engages and supplements the chordwise bending stiffness. But under downward load the lower skin breaks contact with the cantilever, and camber deformation can be achieved at low actuation effort. From two-dimensional ABAQUS™ finite element simulations an upward-to-downward stiffness ratio of 13.82 was obtained with a cantilever extending over the entire length of the conformable section, but the maximum downward camber deflection was limited to 10 deg. Reducing the cantilever length reduced the stiffness ratio but allowed higher maximum camber deformations. A three-dimensional prototype was fabricated using "moderate-length" cantilevers and the measured stiffness ratio (under upward-to-downward loading) was determined to be 5.12. The corresponding stiffness ratio from a three-dimensional ABAQUS finite-element simulation was found to be within 6% of experimental results.

Nomenclature

EI	=	flexural stiffness, N · m^2
F, P	=	applied tip load, N
L	=	length, m
w	=	upward tip displacement, m

I. Introduction

IT IS widely appreciated in the aeronautics community that aircraft wing (or helicopter rotor blade) camber variation can result in improved aerodynamic performance over diverse operating conditions. Offering greater efficiency than the operation of discrete control surfaces (like flaps and ailerons), camber variation can be used for redistribution of lift along the wing or rotor blade, for primary flight control, as well as for gust alleviation and aeroelastic stability problems. From the 1980s to early 2000, major government programs invested significant resources to pursue this technology [1–4]. More recently, NASA proposed a variable camber continuous trailing edge (VCCTE) flap system for control of highly flexible wing structures designed for low-weight and low aerodynamic drag [5].

Beyond the major government demonstration programs a substantial amount of additional research is available in the literature (see, e.g., [6–23]), with the specific approach to achieving trailing-edge camber dependent on the magnitude of the deformation required, its frequency, its spanwise variation, and the specific application. Most of the prior work uses some kind of flexible core/substructure in the morphing region of the airfoil (e.g., [17,18,21–23]), coupled with diverse actuation methods to camber the trailing edge, including shape memory alloys [6–10], piezoelectric actuators [11–16], pneumatic actuators [17], and even conventional servomotors (e.g., [18]). Some studies have also used postbuckled elements [19], skin warping [20], and other mechanisms to amplify the camber deformations. Similarly, another area that has been the subject of much attention over the last several years is the design of high-strain capable flexskins that can simultaneously bear aerodynamic loads and satisfy a range of other constraints [23–28].

One of the fundamental and enduring problems associated with airfoil camber morphing is the requirement that the morphing airfoil/wing/rotor blade section be simultaneously rigid in chordwise bending to minimize uncommanded deformation under aerodynamic load, and at the same time be sufficiently compliant to eschew exorbitant actuation force and actuation energy requirement (which in turn translates to actuator size, weight, and power costs). Although mathematically optimal solutions that seek to simultaneously meet these apparently conflicting objectives have been pursued (see, e.g., [11,12]), the present study takes a more innovative conceptual approach for a specific situation, discussed below. With the upper surface of an airfoil aft of the spar under suction and the lower surface under pressure, the tendency of the aerodynamic loads is to camber the airfoil tail upward (reflex the airfoil). If the actuated camber deflection sought is only in the downward direction (e.g., to generate high lift over a section of the wing or helicopter rotor blade), it could be tremendously advantageous to design the aft airfoil as a structure with a much higher chordwise bending stiffness in the upward direction (to limit deformation under aerodynamic load) and a substantially reduced chordwise bending stiffness in the downward direction (to reduce actuation force requirement). The current study presents a concept that would produce such a difference in chordwise bending stiffness based on direction of load, investigates the performance using finite element analysis, and verifies the simulation results experimentally. The concept could be coupled to a wide range of actuation methods (such as those cited in the previous paragraph), but the actuation method itself is not the focus of the present study.

II. Concept and Analysis

Consider a slender cantilevered beam of length L and flexural stiffness EI subjected to the upward tip load P. From strength of materials, the tip displacement is known to be

$$w = \frac{PL^3}{3EI} \tag{1}$$

Now although the upward load continues to act on the beam, a downward tip load, F ($F > P$), is introduced to reverse the deformation of the beam and cause it to bend down. F can be expressed as

$$F = P + P_1 \tag{2}$$

Received 21 August 2017; revision received 6 November 2017; accepted for publication 7 November 2017; published online 28 December 2017.

*Rotorcraft, Adaptive and Morphing Structures (RAMS) Lab, Department of Mechanical, Aerospace and Nuclear Engineering; dipalm@rpi.edu.

†Rotorcraft, Adaptive and Morphing Structures (RAMS) Lab, Department of Mechanical, Aerospace and Nuclear Engineering; fgandhi@rpi.edu.

where the component P negates the upward force and the component P_1 produces the additional downward deformation from the neutral position. The downward deflection, w_1, is

$$w_1 = \frac{P_1 L^3}{3EI} \tag{3}$$

If the desired downward deflection is $w_1 = \propto w$, it can be shown that $P_1 = \propto P$, and therefore,

$$F = P + \propto P \tag{4}$$

If $\propto = 10$ (a required downward deflection 10 times the deflection under the upward load, P), then clearly, the downward force is 11 times larger than the force P. While the first term on the right-hand side of Eq. (4) is the term required to overcome the upward force, the second term is the dominant component required to overcome structural stiffness to achieve the desired downward deflection.

Now consider the situation where the structural stiffness for downward deformation is reduced by a factor β; then the downward deflection would now be

$$w_1 = \frac{P_1 L^3}{3EI/\beta} \tag{5}$$

If the desired downward deflection is once again $w_1 = \propto w$, then it can be shown that $P_1 = (\propto/\beta)P$, and therefore,

$$F = P + \frac{\propto}{\beta} P \tag{6}$$

If $\propto = 10$, but also $\beta = 10$, then $F = 2P$. The downward force required to produce a downward displacement 10 times as large as the upward displacement is simply twice the magnitude of the upward force, due to the reduced stiffness under downward loading. In Eq. (6), the first term on the right-hand side is the same as Eq. (4). In other words, the upward force must first be canceled out to return the beam back to neutral. But the second term, representing the component that overcomes structural stiffness to push the beam down from neutral, is reduced by a factor β due to the reduced stiffness under downward loading.

The concept described above is sought to be applied to the airfoil chordwise bending (camber) problem. Figure 1 shows a schematic representation of airfoil camber displacement versus upward/downward force. The line AOB (in red) represents the behavior if the airfoil had a very large chordwise bending stiffness. Under an upward aerodynamic force (operating point A), the upward camber deformation would be very small (point A′), as required, due to the high chordwise bending stiffness. However, assuming that the desired downward camber under actuation is substantially larger, putting the airfoil at operating point B, the required actuation force (point B′) is observed to be extremely large due to the high stiffness. Conversely, the line COD (in green) represents the behavior if the airfoil had a very low chordwise bending stiffness. In that case, the desired downward camber displacement (operating point C) could be achieved at a much lower actuation force requirement (point C′). However, the upward camber deformation under aerodynamic load (operating point D) would increase tremendously (point D′). The proposed goal is to operate over the solid portion (OA) of the red curve under upward aerodynamic loads, and over the solid portion (OC) of the green curve at reduced stiffness under downward actuation load. By effectively "bending" the force/displacement curve and operating along COA, the deformation under aerodynamic load remains small (point A′), as does the actuation force to achieve large downward camber (point C′ instead of point B′). Similar to the simple cantilever beam example presented earlier, the magnitude of the actuation force required A′′OC′ comprises of the portion A′′O to overcome aerodynamic load and a smaller component OC′ (compared with OB′) to overcome the reduced chordwise bending stiffness.

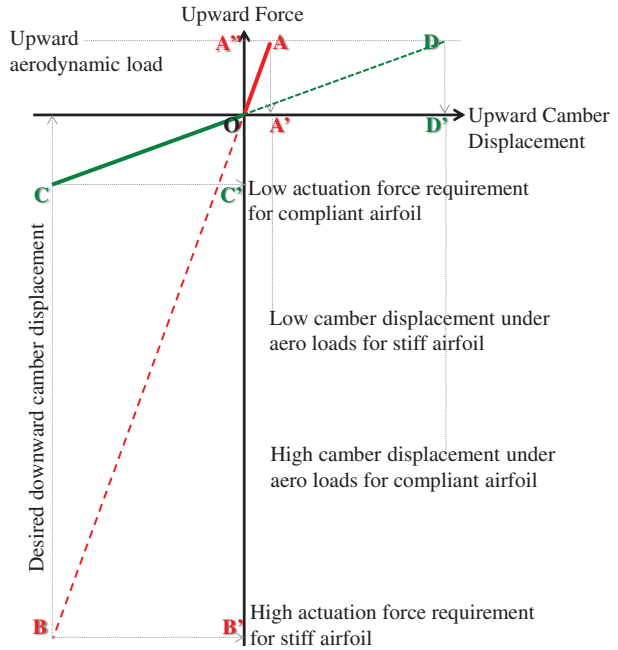

Fig. 1 Schematic representation of airfoil camber displacement versus upward/downward force.

This study explores one particular method for realizing a variable chordwise bending stiffness under upward and downward loading. A NACA 0012 airfoil is chosen for the study, and as shown in Fig. 2, it comprises of a rigid leading-edge D-spar extending from the nose to 32.5% chord, followed by a conformable region extending another 42.5% chord, and finally a solid trailing-edge section over the final 25%. The conformable section comprises of a serial arrangement of vertebrae-like elements (based on [23]) along with a notionally compliant skin, and enables chordwise bending (camber) deformation at modest force. For the calculations in a two-dimensional study conducted first, a concentrated upward or downward force is applied at the point indicated on Fig. 2 at the beginning of the rigid trailing-edge section.

To achieve directional stiffness variation, a rigid cantilever extending from the rear of the spar is introduced adjacent to the camber morphing rib. As shown in Fig. 3 (middle), the underside of the cantilever is in contact with the lower skin in the undeformed configuration. Under upward aerodynamic load, the lower skin (and outer airfoil shell) pushes firmly against the rigid cantilever, which offers a very large resistance (and high stiffness) to upward camber deformation (Fig. 3, top). Conversely, under downward actuation load the lower skin (and outer airfoil shell) disengages from the rigid cantilever (Fig. 3, bottom). With the cantilever offering no resistance to downward camber deformation, the stiffness under actuation load is greatly reduced.

A two-dimensional analysis was first undertaken using the ABAQUS™ finite element analysis software (version 6.13) to evaluate the deformation of the system under concentrated upward and downward forces. The leading-edge spar was assumed to be rigid, as was the trailing-edge section. The conformable section between was assumed to be made out of Delrin® (whose modulus was determined to be 575,000 psi through tensile testing of dog bone coupons). The rigid cantilever, assumed to be geometrically coplanar with the rib, is of aluminum (modulus 10×10^6 psi), and the top skin

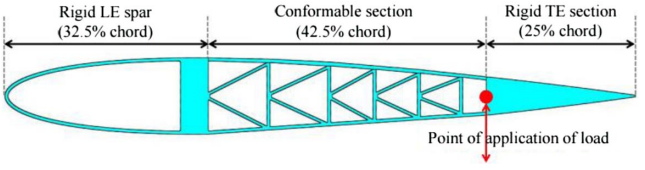

Fig. 2 Camber morphing variant of a NACA 0012 airfoil used for simulations in this study.

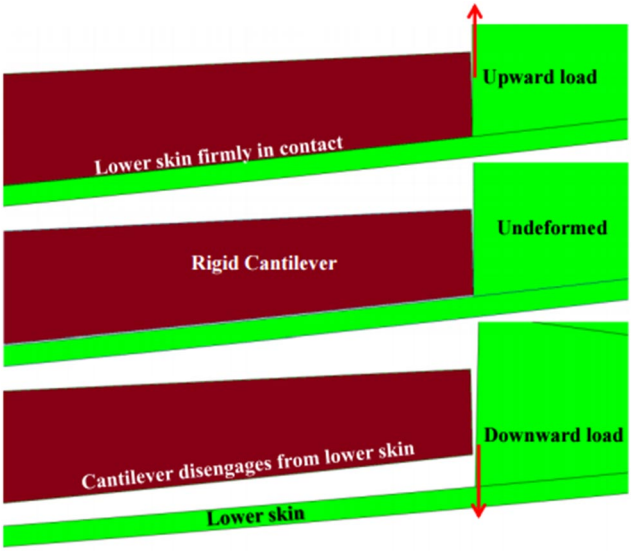

Fig. 3 Rigid cantilever and lower surface skin, in various loading states.

was assumed to have the axial stiffness properties of an elastomer (1200 psi). The ABAQUS model is generated from the Selig point data of a NACA 0012 airfoil, scaled to a chord length of 18 in. The thickness of the structural elements in the vertebrae and that of the lower surface of the rib was 1% chord. The majority of the model was automatically seeded with a mesh consisting of 2D CPS4R 4-node bilinear and CPS3 3-node linear plane strain elements (with reduced integration and hourglass control), whereas the upper skin was modeled with B21 planar beam elements (with linear interpolation) and assigned a cross-sectional geometry to facilitate in plane extension while restricting out of plane bending. In total, 44,395 nodes are used to model the conformable airfoil rib section (including the vertebrae and skin), whereas the number of nodes used to model the aluminum cantilever ranges from 1195 (short cantilever) to 1633 elements (full-length cantilever), and numerical convergence was confirmed. Figure 4 shows the two-dimensional ABAQUS mesh used over a portion of the conformable section. Calculated deformations are obtained under applied (upward and downward) loads. XFOIL panel method analysis was used to compute the pressure on the airfoil at Mach 0.3 and 4 deg angle of attack, and the conversion of the integrated loads over the aft section to an equivalent point force at 75% chord was used to define the range of upward forces (representative of aerodynamic loads) applied on the airfoil. An equivalent camber deformation is calculated as the arctangent of the ratio of the vertical tip deflection to 67.5% chord length (distance from the rear of the leading-edge spar to the trailing-edge). The upward-to-downward bending stiffness ratios are calculated for variations of cantilever length and elastic modulus. The calculated FE deformations are also used to examine the stresses in the vertebrae and the mean strains in the skins.

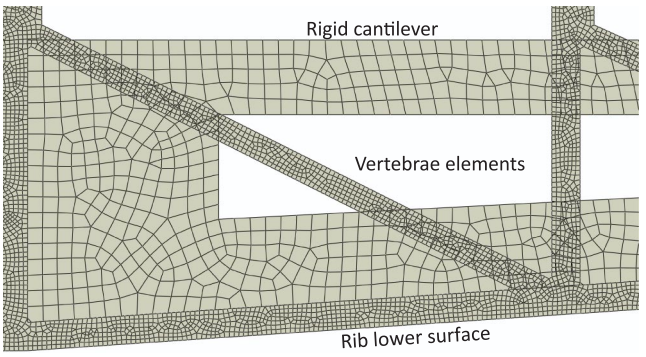

Fig. 4 Two-dimensional ABAQUS mesh used over a portion of the conformable section.

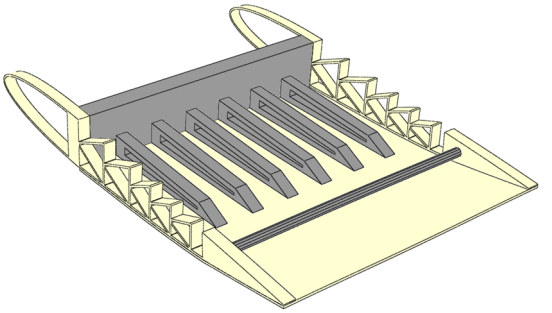

Fig. 5 CAD model of camber morphing wing section with cantilevers.

Following the two-dimensional finite element analysis, a full three-dimensional finite element model was developed to represent a spanwise section shown in Fig. 5. The three-dimensional model comprises a 12-in. span wing section featuring two Delrin NACA 0012 0.5-in.-thick rib sections at either end, and six 0.5-in.-thick aluminum cantilever members distributed evenly along an 11-in. rectangular aluminum spar between. The cross section of the airfoil rib sections is identical to that of the two-dimensional study (Fig. 2), with the omission of the upper skin. A 3/8-in.-diameter aluminum rod is fixed between the trailing edge portions of the ribs for upward and downward load application, and a supplemental Delrin lower skin is attached to the underside of the ribs to span the length of the wing section aft of the spar. The planform dimensions of this wing section are 18 in. along the chord and 12 in. along the span. The model contains over 145,000 linear hexahedral elements (C3D8R), the majority of which are concentrated in the flexible Delrin skin and morphing rib sections. The upward-to-downward bending stiffness ratios were calculated and compared with experimental results.

III. 2D Finite Element Results

The length of the rigid cantilever designed to stiffen the system under upward loading was parametrically varied in this study. Attached to the rear of the rigid leading-edge spar at 32.5% chord, and extending along the chord toward the trailing edge up to 75% chord, the longest cantilever considered extends over the entire conformable region undergoing chordwise bending. Figure 6 shows the airfoil under a downward load when such a full-length cantilever is used. From the figure it is observed that at some magnitude of camber deflection the upper skin comes in contact with the cantilever, thereby preventing further downward camber deflection. The maximum camber achieved with the full-length cantilever was 10 deg. Figure 7 shows ABAQUS simulation results of force versus trailing-edge tip deflection under upward and downward loads. The section of the red line with symbols represents deformation under upward load, whereas the section of the blue line with symbols represents deformation under downward load. Clearly the airfoil is much more compliant under downward deflection, and vice-versa. The stiffness ratio (ratio of the slopes of the portions of the curve under upward and downward loading) is calculated to be 13.82. It should be noted that in the absence of the cantilever, the displacement under upward load would be represented by the extrapolated section of the blue line (shown dashed and without any symbols). The blue line, in general, represents the chordwise bending stiffness of the compliant core (comprising of serially attached vertebrae-like sections) and the upper and lower skin, and its extrapolation represents the contribution of the core and skins to the total stiffness under upward deflection. The difference between the red line with symbols and the blue line without symbols represents the contribution of the

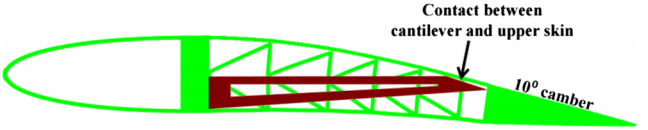

Fig. 6 Airfoil with full-length cantilever under a downward load.

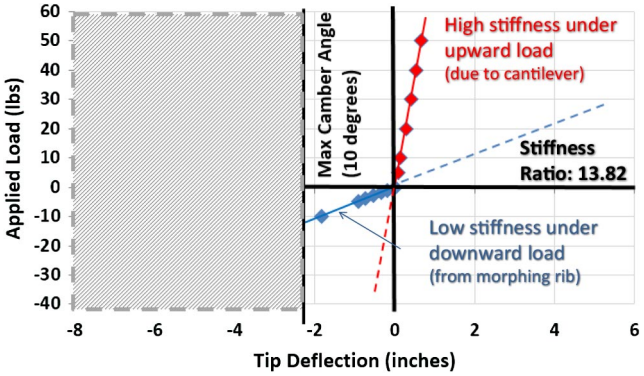

Fig. 7 ABAQUS load versus tip deflection simulation results with full-length cantilever.

cantilever to stiffness under upward deflection. Extrapolation of the red line to the dashed section without any symbols indicates how much larger the required actuation force would be to achieve a desired camber deflection if the stiffness to resist aerodynamic loads was not reduced (by disengagement of the cantilever).

If camber deflections larger than the 10 deg achieved above are required, the length of the cantilever can be reduced. Figure 8 shows the airfoil under a downward load, when a moderate-length cantilever (82% of the full-length cantilever) is used. The upper skin still comes in contact with the cantilever but at a much higher camber deflection (19 deg). Figure 9 shows ABAQUS simulation results of force versus trailing-edge tip deflection under upward and downward loads for the moderate length cantilever. The section of the red line with symbols once again represents deformation under upward load. The section of the blue line with symbols, representing deformation under downward load, is identical to Fig. 7. While the moderate-length cantilever allows a larger maximum camber deflection, the stiffness under upward loading is clearly reduced (compare Fig. 9 with Fig. 7). The stiffness ratio (ratio of the slopes of portions of the curve under upward and downward load) is in this case calculated to be 5.30.

Even larger maximum camber deflections under downward load can be achieved by further reducing the length of the cantilever. Deformation under downward actuation load with the use of a short cantilever (57% of the full-length cantilever) is shown in Fig. 10. At a downward camber deflection of 19 deg, the upper skin is not in

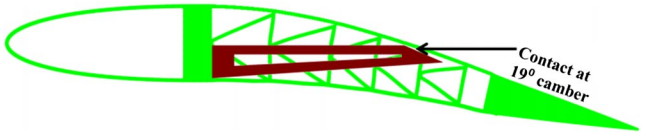

Fig. 8 Airfoil with moderate-length cantilever under a downward load.

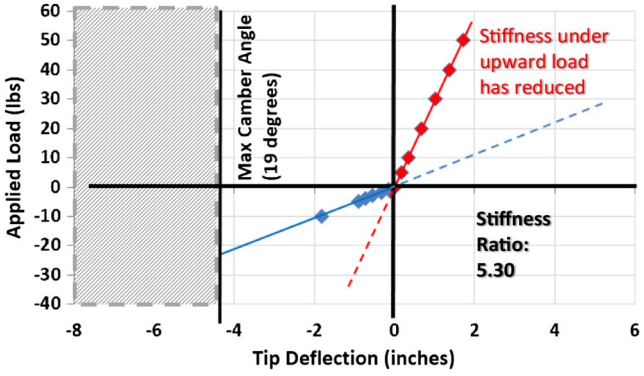

Fig. 9 ABAQUS load versus tip deflection simulation results with moderate-length cantilever.

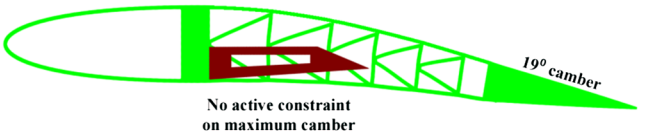

Fig. 10 Airfoil with short-length cantilever under a downward load.

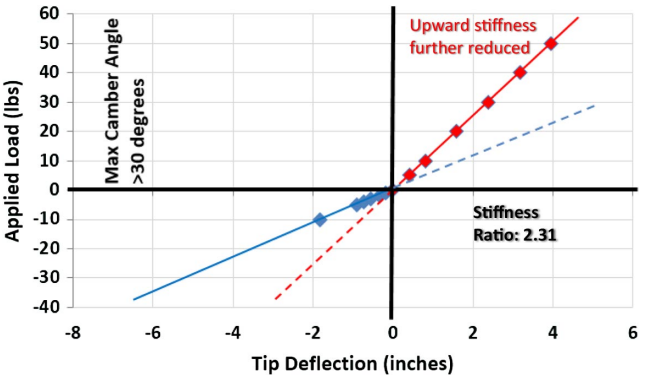

Fig. 11 ABAQUS load versus tip deflection simulation results with short-length cantilever.

proximity of (and at risk of contact with) the cantilever. Figure 11 shows ABAQUS simulation results of force versus trailing-edge tip deflection under upward and downward loads for the short cantilever. The section of the blue line with symbols, representing deformation under downward load, is identical to Figs. 7 and 9. The chordwise bending stiffness under upward load is seen to be further reduced (compare the reduced slope of the red line with symbols in Fig. 11 to Figs. 7 and 9), and the stiffness ratio (ratio of the slopes of the portions of the curve under upward and downward loading) is in this case of the short cantilever calculated to be 2.31. The short cantilever, while relaxing the maximum camber constraints under downward loading, is less effective in stiffening the system under upward loading.

Figure 12 compares the deformation under upward load with the use of the full-length, moderate-length, and short cantilevers. With the full-length cantilever, the rigid trailing-edge region is seen to essentially pivot about the end of the cantilever. For the moderate-length cantilever, the section of the conformable region aft of the cantilever tip is observed to undergo chordwise bending, and the slope at the end of this conformable region carries into the rigid trailing edge. For the short cantilever, the region undergoing chordwise bending is significantly increased, as is the upward trailing-edge tip deflection. From the results in Fig. 12 the reduction in stiffness under upward load with decreasing cantilever length can be attributed to chordwise bending experienced over an increased length of the conformable region aft of the cantilever tip.

In addition to change in cantilever length, the modulus of elasticity of the cantilever was varied. These comparisons were conducted for

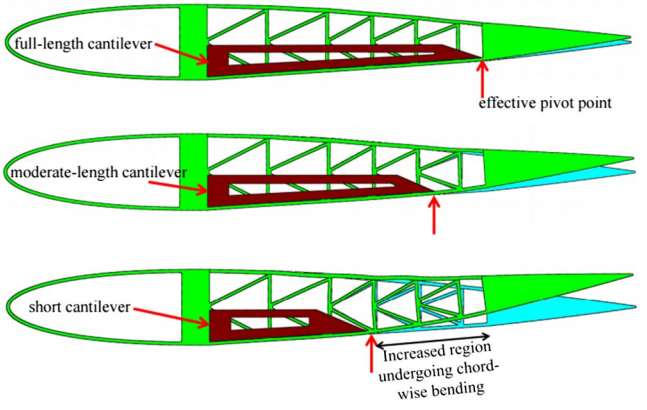

Fig. 12 Deformation under upward load for all three cantilever lengths.

Table 1 Stiffness ratio with variation in cantilever modulus

Percent of baseline cantilever modulus	Stiffness ratio
50	5.15
100	5.30
200	5.39

the moderate-length cantilever. The baseline cantilever was assumed to be made out of aluminum (Young's modulus 10×10^6 psi). ABAQUS simulation results were obtained for a reduced modulus of 5×10^6 psi and with the modulus increased to 20×10^6. The change in stiffness ratio with change in cantilever modulus is presented in Table 1. Clearly, change in cantilever modulus has a relatively small influence on stiffness ratio, compared with change in cantilever length.

Figures 13 and 14, respectively, show the stress distribution in the vertebrae in the conformable section of the airfoil and the strain distribution in the upper skin, corresponding to a 10 deg downward camber deflection. Regions of high stress concentration are observed at the junctions between successive vertebrae in Fig. 13. If the rib was fabricated out of aluminum, the allowable material limits would be reached at a downward camber deformation of about 4 deg. For a rib fabricated out of Delrin™, a 12.5 deg downward camber deflection can be realized before entering the nonlinear stress/strain regime. Of course, structural design modifications to the compliant core could be introduced to achieve the desired camber deformation without violating constraints on the allowable material limits. Indicated on Fig. 14 is the mean strain in segments of the upper skin over individual vertebrae sections. The strain, mostly uniform over a single vertebra, is highest over the second vertebrae, reaching a mean value of 2.3% corresponding to a 10 deg downward camber. The strain levels in the skin play an important role in skin material selection. The strain in any skin segment is related to the relative rotation between adjacent vertebrae, with greater relative rotation leading to larger strains in the skin segment between. The maximum skin strains can be reduced by limiting the relative rotation between successive vertebrae through structural optimization, while still realizing a specified camber deformation. The current study uses an *ad hoc* vertebrae design, with no effort directed to reduction in maximum skin strains or stress concentrations at the vertebrae junctions.

IV. 3D Finite Element Results

The three-dimensional analysis confirms the trends observed from the two-dimensional simulations, but also illustrates several interesting three-dimensional phenomena that the previous simulations could not capture. Figure 15 depicts the relationship between tip displacement versus applied load for the moderate-length cantilever. The upward-to-downward stiffness ratio for the moderate-length cantilever was 4.83. In the three-dimensional simulation, the upward and downward load was applied as a concentrated force at the midpoint of the rod running along the span, close to the trailing edge, as was the case in the experiment (described in Sec. V). At a large upward load of 10 lbs the simulation indicates that the rod and the lower skin both undergo spanwise bending, as seen in Fig. 16 (displacements amplified by a factor of 3 for clarity). The spanwise bending of the skin results in the outermost cantilevers (closest to the ribs) being the only ones resisting the upward deformation of the skin, while the four central cantilevers are rendered inactive. This phenomenon is observed in the stress distribution in Fig. 17, where stress concentration "hot spots" are visible at the tips of only the outermost cantilevers. The spanwise bending puts the system in the lowest energy state and the stiffness under upward loading is reduced somewhat. Suppression of spanwise bending in the skin (through an *ad hoc* increase in skin stiffness in the spanwise direction, for example) was seen to increase the stiffness under upward loading. Similarly, a slight increase in stiffness under upward loading was also observed by moving the outermost cantilevers closer to the ribs. A distributed pressure loading such as would be encountered due to aerodynamic loading during actual operation (compared with the concentrated load applied at the center of the rod) would suppress the spanwise bending mode discussed above, and all the cantilevers would be engaged in stiffening the system under upward load.

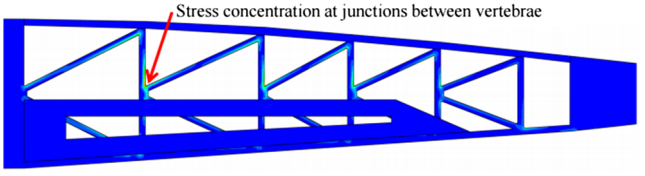

Fig. 13 Stress distribution in conformable vertebrae for 10 deg downward camber deflection.

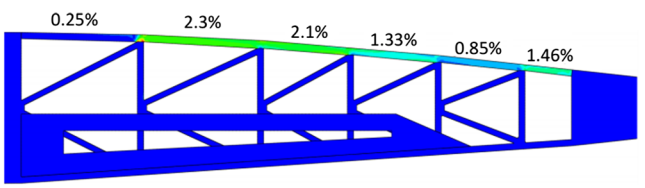

Fig. 14 Strain distribution in upper skin in conformable section for 10 deg downward camber.

V. Prototype Design, Fabrication, Assembly, and Experimental Setup

An experimental prototype, identical to the three-dimensional CAD and finite element model, was fabricated to validate the bi-directional stiffness characteristics of the concept presented in this study. Two 18-in.-chord, 0.5-in.-deep NACA 0012 rib sections were fabricated from Delrin Acetal Resin using a water jet cutter (Fig. 18). The structural elements in these ribs over the morphing section

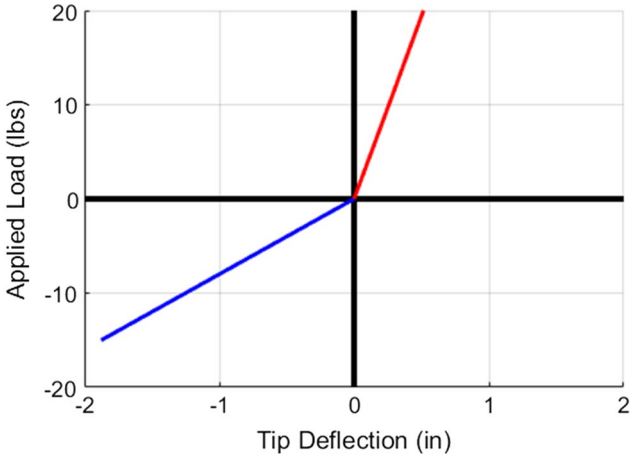

Fig. 15 ABAQUS 3D simulation results for load versus tip deflection with moderate-length cantilever.

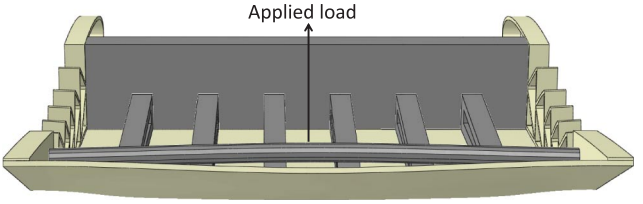

Fig. 16 Spanwise bowing of lower skin under 10 lbs load, magnified (3×) for clarity.

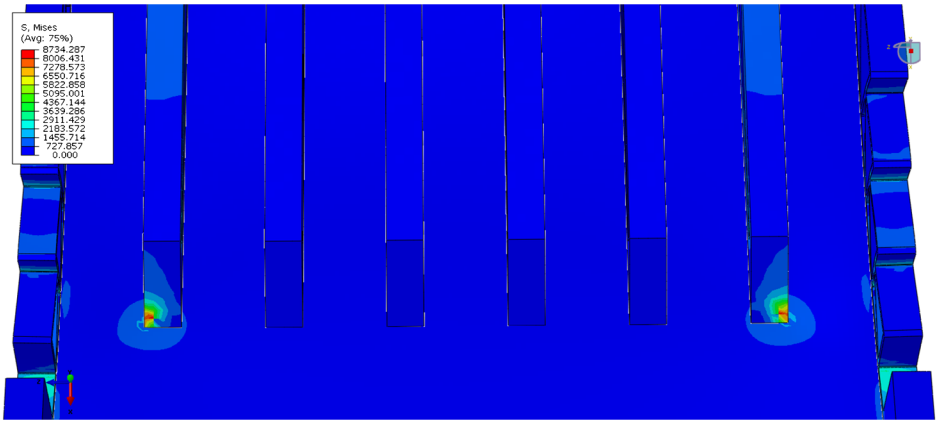

Fig. 17 Von Mises stress distribution from 3D ABAQUS FEA.

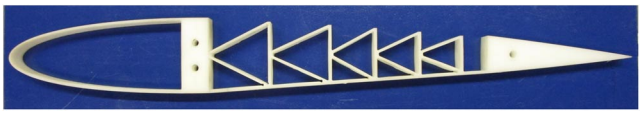

Fig. 18 Water jet cut Delrin Acetal Resin NACA 0012 rib section.

(extending between 32.5% and 75% chord) have a thickness of 1% chord. The ribs also feature filled solid regions at 30% chord for a $0.05c$ thickness spar and over the last 25% chord at the trailing edge. The solid sections of the ribs at 30% chord are bolted at either end of an 11 in. × 1 in. × 2.5 in. block of 6061 aluminum that serves as the spar and the base foundation for the entire assembly. The underside of the ribs, aft of the spar, is bolted to a 12-in. square 3/32-in.-thick Delrin Acetal Resin sheet that will serve as the lower skin of the entire wing section. The trailing edge portions of the ribs are bolted to a 3/8-in.-diameter 6061 aluminum rod, at the center of which force is applied during the test. Six "moderate-length" cantilevers were water jet cut from a ½-in.-thick block of 6061 aluminum. These six cantilevers were bolted equidistant from one another to the aft side of the aluminum spar, such that they were flush in-contact with the lower skin in an unloaded state.

For testing purposes, the aluminum spar was clamped to a heavy table, with the trailing edge of the airfoil extending past the edge of the table with adequate room to camber downward without any interference. A steel cable was woven through a hole drilled at the center of the aluminum rod at the trailing edge of the prototype. For application of a downward load, the cable was threaded through a small hole cut in the Delrin lower skin with weights applied at the free end of the cable in increments and the corresponding trailing edge vertical displacements measured. Figure 19 shows an image of the experimental setup under a downward load. To measure the deformation under upward load the prototype was simply inverted, as shown in Fig. 20.

VI. Experimental Results and Comparison with 3D FEA

The measured displacement of the prototype under upward and downward load shows good overall correlation with the three-

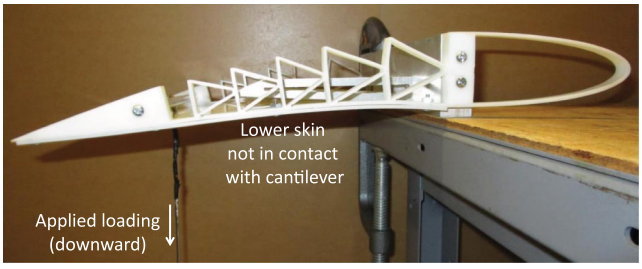

Fig. 19 Experimental setup to measure tip displacement under a downward load.

Fig. 20 Prototype inverted to measure tip displacement under "upward" load.

dimensional finite element results, as seen in Fig. 21. The experimental data show a slight softening behavior compared with the FEA simulation results (dashed lines). Evaluated over a range extending from −5 to +5 lbs applied load, the experimentally evaluated stiffness ratio under upward-to-downward load was 5.12 (a difference of 6% compared with the stiffness ratio of 4.83 from the 3D FEA simulations). A closer examination further reveals that under upward loading, the stiffness predicted from the 3D FEA simulation is within 1% of the experimentally measured stiffness over the 0 to 5 lbs range. Under downward load, the discrepancy over the 0 to −5 lbs range was slightly greater, with the stiffness predicted from 3D FEA simulation 4.85% larger than experimentally measured.

While small differences between simulation and test can be attributed to imperfections in fabrication, assembly, and boundary conditions, the experimentally observed nonlinear softening behavior was examined further. Figure 22 shows the simulated

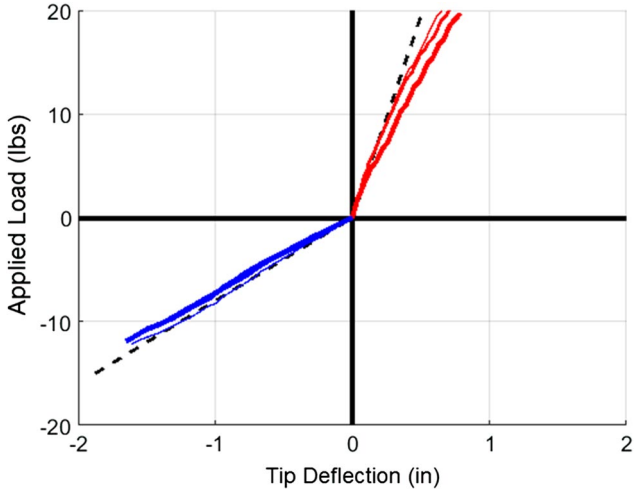

Fig. 21 Experimental force–displacement trends (3 trials) plotted against the FEA results.

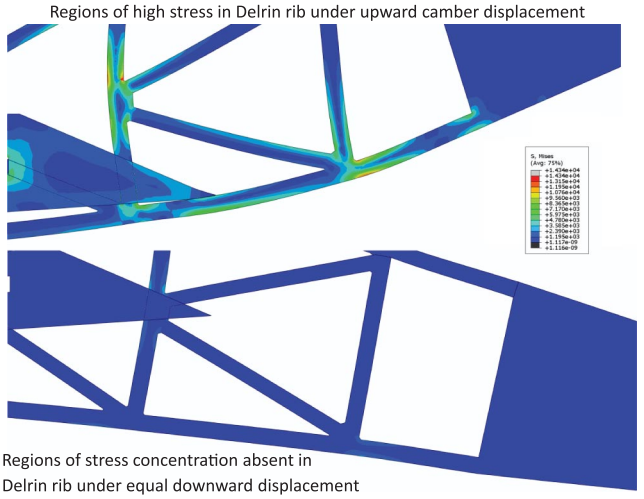

Fig. 22 Stress distribution in the aft section of the morphing region of the rib, under upward and downward load.

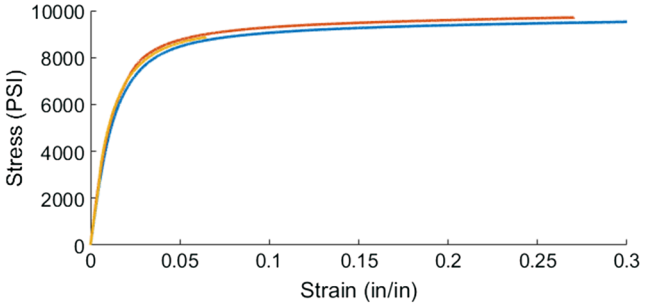

Fig. 23 Experimentally measured stress versus strain behavior of the Delrin material used in the experiment.

stress distribution in the aft section of the morphing region of the rib, under both upward and downward loading for equal overall camber deflections. Under downward loading, the deformation in the rib is more uniform over the entire morphing region. On the other hand, with the moderate-length cantilever suppressing chordwise bending over the front section of the morphing region under upward loading, significantly larger stresses are observed over the aft section of the rib's morphing region (consistent with the earlier discussion related to Fig. 12). Figure 23 shows the experimentally measured stress versus strain behavior of the Delrin material used in the experiment from which a modulus of 575,000 psi was determined corresponding to the low-strain regime. However, it is clear that at high strains the material softens, and because high strains in the Delrin are more prevalent under upward loading the softening phenomenon in the force/displacement characteristics (at increasing load) seen in Fig. 21 is also more prominent under upward load.

Additionally, it should be noted that the phenomenon of bowing of the lower skin and lower skin contact with only the cantilevers closest to the ribs under upward load, as shown in Figs. 16 and 17, was experimentally verified (results not included in the paper).

VII. Conclusions

Aerodynamic loads on an airfoil (suction on the upper surface and pressure on the lower surface) tend to camber the region aft of the spar upward in normal operating conditions. In many applications, downward camber deflections are sought for high-lift or load redistribution. This paper focuses on the design of the aft section of an airfoil that is very stiff under upward loading but much more compliant under downward loading, so that the deformation under aerodynamic loading is very small, but the actuation force requirement to camber downward is modest, as well. The design uses rigid cantilever members extending from the rear of the spar toward the trailing edge, flush with the lower skin of the airfoil. Under upward load (representative of aerodynamic pressure), the rigid cantilever engages and supplements the stiffness of the wing to resist upward camber deformation. But under downward load (representative of an actuated state), the lower skin breaks contact with the cantilever, and camber deformation can be achieved at low actuation effort. Two-dimensional and three-dimensional ABAQUS finite element simulations were conducted for the system with bi-directional camber stiffness, and the three-dimensional simulation results were validated against experimental. From the results in this study the following conclusions were drawn:

1) For a "full-length" cantilever extending over the entire length of the conformable section (between the leading edge D-spar and the trailing edge section), the effective stiffness under upward loading was calculated to be 13.82 times the stiffness under downward loading using 2D finite element simulation. But the maximum camber deformation was limited to 10 deg due to contact between the cantilever and the upper skin.

2) A "moderate-length" cantilever extending over 82% of the length of the conformable section allowed a larger maximum camber deformation (19 deg) but the stiffness under upward load reduced (ratio of upward-to-downward stiffness reduced to 5.30).

3) A "short" cantilever extending over 57% of the length of the conformable section effectively eliminated any constraint on downward camber deformation, but the stiffness under upward load further reduced (with the stiffness ratio down to 2.31).

4) Reduction in effective stiffness under upward load with reduced cantilever length is attributed to bending deformation over the portion of the conformable section between the cantilever tip and the beginning of the trailing edge section.

5) Changes in cantilever modulus had a smaller effect on the stiffness ratio than changes in cantilever length. Using a moderate-length cantilever, reducing the modulus to half that of aluminum reduced the stiffness ratio from 5.30 to 5.15, whereas increasing the modulus to double that of aluminum increases the stiffness ratio to 5.39.

6) A three-dimensional prototype was fabricated using "moderate-length" cantilevers and the measured stiffness ratio (under upward-to-downward loading) was determined to be 5.12. The corresponding stiffness ratio from three-dimensional finite-element simulation was found to be within 6% of experimental results.

References

[1] Hall, J., "Executive Summary AFTI/F-111 Mission Adaptive Wing," Wright Research Development Center, Technical Rept. WRDC-TR-89-2083, Wright–Patterson Air Force Base, 1989.

[2] Pendleton, E. W., Bessette, D., Field, P. B., Miller, G. D., and Griffin, K. E., "Active Aeroelastic Wing Flight Research Program: Technical Program and Model Analytical Development," *Journal of Aircraft*, Vol. 37, No. 4, 2000, pp. 554–561. doi:10.2514/2.2654

[3] Kudva, J., "Overview of the DARPA Smart Wing Project," *Journal of Intelligent Material Systems and Structures*, Vol. 15, No. 4, 2004, pp. 261–267. doi:10.1177/1045389X04042796

[4] Bartley-Cho, J. D., Wang, D. P., Martin, C. A., Kudva, J. N., and West, M. N., "Development of High-Rate, Adaptive Trailing Edge Control Surface for the Smart Wing Phase 2 Wind Tunnel Model," *Journal of Intelligent Material Systems and Structures*, Vol. 15, No. 4, 2004, pp. 279–291. doi:10.1177/1045389X04042798

[5] Nguyen, N., and Urnes, J. Sr., "Aeroelastic Modeling of Elastically Shaped Aircraft Concept via Wing Shaping Control for Drag Reduction," *AIAA Atmospheric Flight Mechanics Conference*, AIAA Paper 2012-4642, Aug. 2012.

[6] Strelec, J. K., Lagoudas, D. C., Khan, M. A., and Yen, J., "Design and Implementation of a Shape Memory Alloy Actuated Reconfigurable Airfoil," *Journal of Intelligent Material Systems and Structures*, Vol. 14, Nos. 4–5, 2003, p. 257–273. doi:10.1177/1045389X03034687

[7] Barbarino, S., Pecora, R., Lecce, L., Concilio, A., Ameduri, S., and De Rosa, L., "Airfoil Structural Morphing Based on S.M.A. Actuator Series: Numerical and Experimental Studies," *Journal of Intelligent Material Systems and Structures*, Vol. 22, No. 10, July 2011, pp. 987–1004. doi:10.1177/1045389X11416032

[8] Pecora, R., Barbarino, S., Concilio, A., Lecce, L., and Russo, S., "Design and Functional Test of a Morphing HighLift Device for a Regional Aircraft," *Journal of Intelligent Material Systems and Structures*, Vol. 22, No. 10, July 2011, pp. 1005–1023. doi:10.1177/1045389X11414083

[9] Ameduri, S., Brindisi, A., Tiseo, B., Concilio, A., and Pecora, R., "Optimization and Integration of Shape Memory Alloy (SMA)-Based Elastic Actuators Within a Morphing Flap Architecture," *Journal of Intelligent Material Systems and Structures*, Vol. 23, No. 4, March 2012, pp. 381–396. doi:10.1177/1045389X11428672

[10] Bil, C., Massey, K., and Ermira, J. A., "Wing Morphing Control with Shape Memory Alloy Actuators," *Journal of Intelligent Material Systems and Structures*, Vol. 24, No. 7, May 2013, pp. 879–898. doi:10.1177/1045389X12471866

[11] Anusonti-Inthra, P., Sarjeant, R., Frecker, M., and Gandhi, F., "Design of a Conformable Rotor Airfoil Using Distributed Piezoelectric Actuators," *AIAA Journal*, Vol. 43, No. 8, Aug. 2005, pp. 1684–1695. doi:10.2514/1.1519

[12] Gandhi, F., Frecker, M., and Nissly, A., "Design Optimization of a Controllable Camber Rotor Airfoil," *AIAA Journal*, Vol. 46, No. 1, 2008, pp. 142–153. doi:10.2514/1.24476

[13] Grohmann, B., , Maucher, C., and Prunhuber, T.et al., "Multidisciplinary Design and Optimization of Active Trailing Edge for Smart Helicopter Rotor Blade," *Mechanics of Advanced Materials and Structures*, Vol. 15, No. 3, 2008, pp. 307–324. doi:10.1080/15376490801907830

[14] Bilgen, O., Kochersberger, K. B., Inman, D. J., and Ohanian, O. J., III, "Macro-Fiber Composite Actuated Simply Supported Thin Airfoils," *Smart Materials and Structures*, Vol. 19, No. 5, 2010, Paper 055010. doi:10.1088/0964-1726/19/5/055010

[15] Bilgen, O., Kochersberger, K. B., Inman, D. J., and Ohanian, O. J., "Novel, Bidirectional, Variable Camber Airfoil via Macro-Fiber Composite Actuators," *Journal of Aircraft*, Vol. 47, No. 1, 2010, pp. 303–314. doi:10.2514/1.45452

[16] Bernhammer, L. O., Teeuwen, S. P. W., De Breuker, R., van der Veen, G. J., and van Solingen, E., "Gust Load Alleviation of an Unmanned Aerial Vehicle Wing Using Variable Camber," *Journal of Intelligent Material Systems and Structures*, Vol. 25, No. 7, May 2014, pp. 795–805. doi:10.1177/1045389X13511010

[17] Woods, B. K. S., Friswell, M., and Wereley, N., "Advanced Kinematic Tailoring for Morphing Aircraft Actuation," *AIAA Journal*, Vol. 52, No. 4, April 2014, pp. 798–788. doi:10.2514/1.J052808

[18] Yokozeki, T., Sugiura, A., and Hirano, Y., "Development of Variable Camber Morphing Airfoil Using Corrugated Structure," *Journal of Aircraft*, Vol. 51, No. 3, 2014, pp. 1023–1029. doi:10.2514/1.C032573

[19] Ursache, N. M., Keane, A. J., and Bressloff, N. W., "Design of Postbuckled Spinal Structures for Airfoil Camber and Shape Control," *AIAA Journal*, Vol. 44, No. 12, 2006, pp. 3115–3124. doi:10.2514/1.22636

[20] Mistry, M., and Gandhi, F., "Design, Fabrication and Benchtop Testing of a Helicopter Rotor Blade Section with Warp-Induced Spanwise Camber Variation," *Journal of Intelligent Material Systems and Structures*, Vol. 26, No. 10, 2014, pp. 1272–1289. doi:10.1177/1045389X14541491

[21] Campanile, L. F., and Sachau, D., "The Belt-Rib Concept: A Structronic Approach to Variable Camber," *Journal of Intelligent Material Systems and Structures*, Vol. 11, No. 3, 2000, pp. 215–224. doi:10.1106/6H4B-HBW3-VDJ8-NB8A

[22] Campanile, L. F., Keimer, R., and Breitbach, E. J., "The 'Fishmouth' Actuator: Design Issues and Test Results," *Journal of Intelligent Material Systems and Structures*, Vol. 15, No. 10, 2004, pp. 711–719. doi:10.1177/1045389X04044452

[23] Gandhi, F., and Anusonti-Inthra, P., "Skin Design Studies for Variable Camber Morphing Airfoils," *Smart Materials and Structures*, Vol. 17, No. 1, Feb. 2008, Paper 015025. doi:10.1088/0964-1726/17/01/015025

[24] Olympio, K. R., and Gandhi, F., "Flexible Skins for Morphing Aircraft Using Cellular Honeycomb Cores," *Journal of Intelligent Material Systems and Structures*, Vol. 21, No. 17, Nov. 2010, pp. 1719–1735. doi:10.1177/1045389X09350331

[25] Olympio, K. R., and Gandhi, F., "Zero-Poisson's Ratio Cellular Honeycombs for Flexskins Undergoing One-Dimensional Morphing," *Journal of Intelligent Material Systems and Structures*, Vol. 21, No. 17, Nov. 2010, pp. 1737–1753. doi:10.1177/1045389X09355664

[26] Olympio, K. R., Gandhi, F., Asheghian, L., and Kudva, J., "Design of a Flexible Skin for a Shear Morphing Wing," *Journal of Intelligent Material Systems and Structures*, Vol. 21, No. 17, Nov. 2010, pp. 1755–1770. doi:10.1177/1045389X10382586

[27] Murray, G., Gandhi, F., and Bakis, C., "Flexible Matrix Composite Skins for One-Dimensional Wing Morphing," *Journal of Intelligent Material Systems and Structures*, Vol. 21, No. 17, Nov. 2010, pp. 1771–1781. doi:10.1177/1045389X10369719

[28] Thill, C., Etches, J., Bond, I., Potter, K., and Weaver, P., "Morphing Skins," *The Aeronautical Journal*, Vol. 112, No. 1129, March 2008, pp. 117–139. doi:10.1017/S0001924000002062

R. Ohayon
Associate Editor